buildings

MDPI

Article

Investigation on the Deformation of Segment Linings in Cross-Fault Tunnel Considering the Creep Behavior of Surrounding Rock during Construction-Operation Period

Yinpeng He [1], Xinjian Sun [2,3,*] and Mengxi Zhang [1]

[1] State Key Laboratory of Hydraulic Engineering Simulation and Safety, Tianjin University, Tianjin 300350, China
[2] School of Water Resources and Electric Power, Qinghai University, Xining 810016, China
[3] Laboratory of Ecological Protection and High Quality Development in the Upper Yellow River, School of Water Resources and Electric Power, Qinghai University, Xining 810016, China
* Correspondence: sunxj@qhu.edu.cn

Abstract: Time-dependent deformation of surrounding rocks during construction and service directly affects the structural safety of hydraulic tunnels. Specifically, the creep effect on the cross-fault diversion tunnels is particularly significant. In recent years, a variety of research has focused on the impact of creep on operating cross-fault diversion tunnels. However, there is a lack of consideration for the creep phenomenon during the construction-operation period. This study proposes a simulation method of segment linings deformation of cross-fault diversion tunnel combining deformation monitoring, creep constitutive identification, and creep during construction operation. According to the measured time-displacement data of the surrounding rock, the suitable creep constitutive model is selected by a regression-comparison method. Subsequently, the three-dimensional numerical model of the cross-fault tunnel is established, with the tunnel excavation and long-term creep calculation carried out under the creep effect of the surrounding rock. In addition, the intelligent inversion model was adopted to obtain the basic parameters of the surrounding rock. The results show that fault directly affects the rock mass characteristics near the fault. The radius of influence is about one time the tunnel diameter from the fault. The vertical deformation of segment linings of the vault and inverted arch tends to be subsidence when the fault is above the tunnel; however, the trend is inverse when the fault is under the tunnel. This work gives targeted engineering suggestions and provides a scientific basis for designing and constructing diversion tunnels under complicated geological structures.

Keywords: tunnel engineering; fault; construction-operation period; creep; segment lining; numerical simulation

Citation: He, Y.; Sun, X.; Zhang, M. Investigation on the Deformation of Segment Linings in Cross-Fault Tunnel Considering the Creep Behavior of Surrounding Rock during Construction-Operation Period. *Buildings* **2022**, *12*, 1648. https://doi.org/10.3390/buildings12101648

Academic Editor: Gianfranco De Matteis

Received: 6 August 2022
Accepted: 3 October 2022
Published: 10 October 2022

1. Introduction

Tunnel engineering has been widely used in water transfer projects and has the ability to cross various terrains. This approach can also shorten and smooth the route curve and resist earthquake disasters [1,2]. Generally, hydraulic tunnels are long and extend along with complex geological conditions [3]. In practice, the geology and route limitations inevitably lead to tunnels passing through faults. Moreover, tunnels are surrounded by rocks during construction and operation. In this situation, the influence of the creep of the surrounding rock on the safety of tunnels cannot be ignored. Therefore, the tunnel is prone to collapse and water gushing slightly carelessly and may cause severe financial and material losses as well as personal injury and death [4–6].

In recent years, numerous research has been carried out to evaluate the interaction between cross-fault tunnels and faults, including numerical simulation [7,8], theoretical analysis [9] and model test [10–12]. All the damages to the eight traffic and water conveyance tunnels in Japan, the United States, and Turkey are caused by faults [13]. In

general, the damage in traffic tunnels includes dense cracks in all linings, severe deformation, subsidence, crown bending due to the soil pressure, flaking of the internal surface leading to breakage, peeling concrete blocks, rail deformations, buckling rails, and water gushing. The damage to water conveyance tunnels consists of excessive stress in the tunnel, cracking of walls, and breaking into small and large pieces, which, in turn, reduce the area of tunnel section and form a water hammer. The nonlinear failure process of the strain and fracture behavior of the tunnel-fault system can be divided into five main stages: (1) strain localization, (2) fracture initiation, (3) crack acceleration, (4) spontaneous crack growth, and (5) stability [14]. Several works have been carried out to evaluate the damage in the tunnel, including an evaluation of stress and displacement caused by the fault using a tunnel with an aluminum cylinder in a centrifugal experiment [15], an assessment of dynamic characteristics of the cross-fault tunnel by using the shaking table test [16], and a simulation of the LongMenShan Fault dislocation using a large-scale plate thrust model [17]. Those studies found that the tunnel structure would experience two-stage seismic damage due to the fault movement and seismic motion, where the fault movement contributed to more serious damage to the tunnel structure than seismic motion. Moreover, the articulated design may be adopted and constructed using basalt fiber reinforced concrete (BFRC) material to obtain the tunnel response in order to cope with the serious damage caused by fault dislocation. In order to use this material, the appropriate ratio of BFRC needs to be selected to improve the anti-fault ability.

The above-mentioned investigations have clearly explained the tunnel's failure mode and development process and its supporting system by fault and put forward some measures to enhance the structural performance. In addition, scholars tried to explore the parameters that may affect the structure of cross-fault tunnels from the perspectives of tunnel and fault. For instance, a scale model test was used to evaluate the influence of reverse fault on the failure mode of the tunnel by verifying the test results using a numerical model [18]. This study showed that the essential fault parameters influencing the stability of the tunnel structure are the location, dip angle, thickness of the fault, and distance from the fault and the tunnel. An experimental analysis was performed from the viewpoint of location, depth and stiffness of the tunnel, and the soil relative density. Moreover, they simulated the interaction between the tunnel and sand and proposed that the interaction mechanism between the tunnel and soil should be considered in the tunnel design near the active fault zone [19,20]. Moreover, the influence of faults with different thicknesses and locations on the deformation, stress and plasticity of the tunnel were assessed [21] and further improved the adopted model to discuss the influence of geometric characteristics, i.e., fault angle, fault displacement, tunnel diameter, lining thickness, and overburden depth on the cross-fault tunnel [22]. In addition, the behavior of the tunnel is then analyzed from the perspective of bending moment and axial force combined with the demand-capacity ratio. Similarly, numerical simulations were also used for parametric studies focusing on the performance of shotcrete and segmented lining in shallow tunnels crossing strike-slip faults [23] and influencing factors of the cross-fault tunnel and active length [24].

Significant research works in evaluating the quality of cross-fault tunnels have been carried out, but those studies were mainly focused on instantaneous effects [25]. On the other hand, the influence of segment lining in construction-operation cross-fault tunnel under the creep effect of surrounding rock is widespread. This phenomenon also has an important impact on the long-term stability of cross-fault tunnels [26]. However, the existing literature investigating this phenomenon is still less. Therefore, a numerical simulation method is proposed in this paper to study the creep deformation of segment linings of a cross-fault tunnel from the construction period to the operation period. Moreover, a three-dimensional numerical model of the cross-fault tunnel is established in conjunction with the "Yinda Jihuang" diversion tunnel project (DT-HS project). Among them, the relationship between fault and the deformation of segment linings in the transition section is the key analysis. The research results can provide a reference for the design, maintenance, and operation monitoring of the cross-fault water conveyance tunnels.

2. Overall Framework

Rock mass is regarded as an equivalent continuum [27]. The selected finite difference software FLAC3D can simulate elastic deformation, plastic deformation, plastic flow, strain softening, rheological deformation, and even large deformation of materials [28,29]. Figure 1 is an architecture description of simulation analysis of cross-fault tunnel considering creep effect.

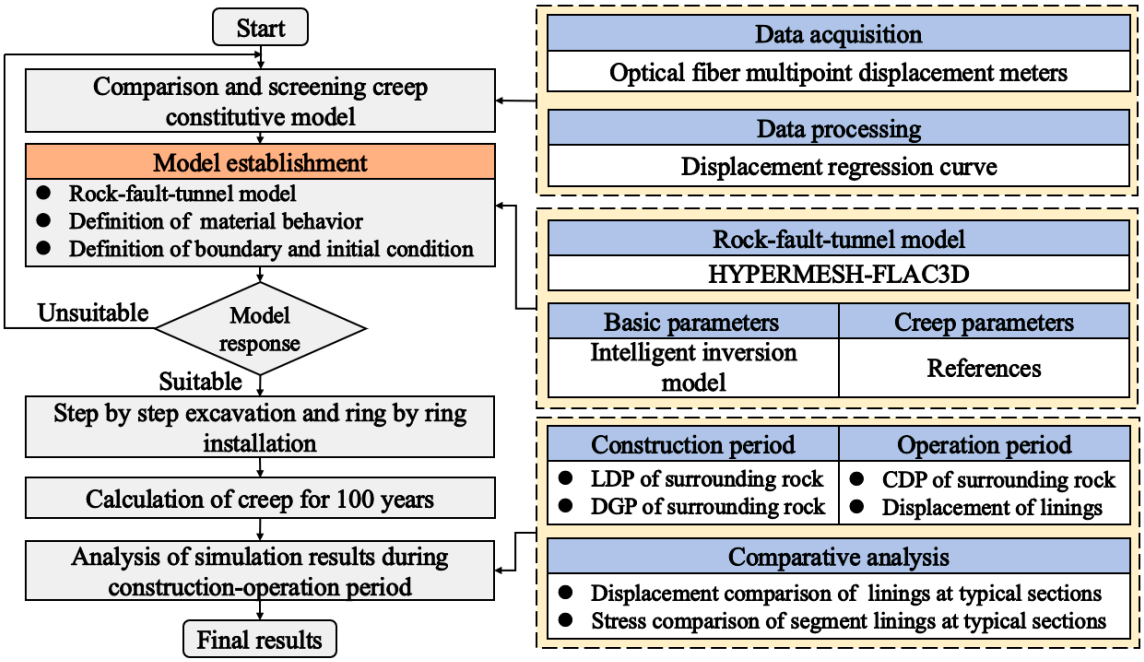

Figure 1. An architecture description of simulation analysis of cross-fault tunnel considering creep effect.

The specific calculation steps are as follows:

(1) Conducting a comparative analysis of the characteristics of several different creep constitutive models and the time-displacement curve of the surrounding rock fitted by using field measured displacement data to select a suitable constitutive model.

(2) Establishing a three-dimensional numerical model with a rock-fault tunnel to calculate the initial stress field. Definitions of material behavior, boundary, and initial condition are used for the balancing calculation.

(3) Simulating tunnel excavation and applying segment lining. In this phase, the displacement produced in calculating the initial stress field needs to be removed to eliminate its influence. The surrounding rock and fault are then set as the constitutive creep model selected in (1), and the corresponding creep parameters are given. Finally, the creep calculation is started. Considering the actual construction process of TBM, with the excavation going on, the segments are arranged ring by ring.

(4) Recording the creep calculation lasted for 100 years, and deformation of surrounding rocks and segment linings after excavation. In order to facilitate the analysis of displacement during operation, the displacement during construction should be cleared at the beginning of this step.

3. Comparison and Screening Creep Constitutive Model

3.1. Component Combination Method

The creep behavior of rocks shows the specific relation of stress-strain-time with great differences in the creep properties of different rocks [30,31]. Various works have been conducted to describe the constitutive relationship of rock creep with a clear concept and physical meaning. The component combination model is one of the widely used methods [32].

In this work, the component of the combination model combines elastic components, viscous components, and plastic components in series or parallel to simulate the elastic, viscous, and plastic behavior of rocks [33]. The distribution of strain, strain rate, and load on each component of the new component combination models are similar to that of the circuit. In other words, the displacement rate and strain are equal to the current, and the load is equal to the voltage. Specifically, in the series models, each component's strain and strain rate are equal, and the total load is the sum of the loads of each component. In the parallel models, the load of each component is equal, and the total strain is the sum of the strains of each component.

The research and application of component combination models have been very extensive [34–38]. Seven common component combination models have been developed including Maxwell, Kelvin, Modified Kelvin, Poying-Thomson, Burgers, Nishihara, and Bingham. Table 1 lists the properties and applicability of each constitutive model.

Table 1. Properties and application scope of common component combination models.

Constitutive	Typical Properties	Scope of Application
Maxwell	Instantaneous strain, steady creep, delayed elasticity	Rocks with larger depths
Kelvin	steady creep, decay creep, delayed elasticity	General rocks
Modified Kelvin	Instantaneous strain, decay creep	Short-term loaded rocks
Poying-Thomson	Instantaneous strain, decay creep	Slate, shale, sandstone, etc.
Burgers	Instantaneous strain, steady creep, decay creep, delayed elasticity	sandstone, mudstone, etc.
Nishihara	$\sigma < \sigma_s$ Instantaneous strain, decay creep $\sigma \geq \sigma_s$ Instantaneous strain, steady creep, decay creep	Soft rock
Bingham	$\sigma < \sigma_s$ Instantaneous strain $\sigma \geq \sigma_s$ Instantaneous strain, steady creep	Clay, semi-hard rock

As shown in Table 1, all models are composed of essential components connected in series and parallel, similar in composition and structure. However, the creep characteristics of models displayed by different combinations are pretty different. Nishihara and Burgers' creep constitutive models can reflect more creep characteristics, so they have a more comprehensive application range. At the same time, Burgers has fewer parameters than Nishihara, which makes it easier to identify parameters. The characteristic creep curves of the commonly used combination models are summarized in Figure 2. The tunnel of the DT-HS project is a deep and extra-long tunnel with extremely high ground stress; hence, only the part of high ground stress for Nishihara and Poying-Thomson is presented in Figure 2. The creep deformation of Kelvin, Modified Kelvin, and Poying-Thomson remains constant after reaching a certain time, while the creep deformation of other models will continue to increase.

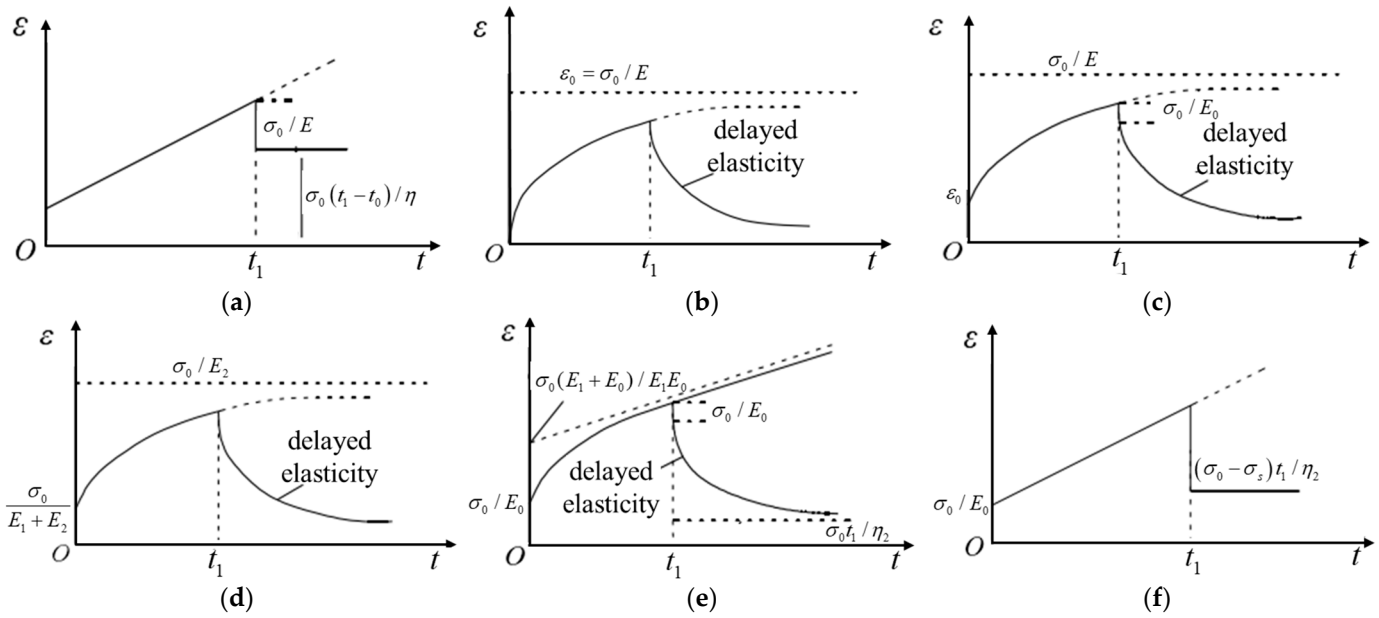

Figure 2. Creep characteristic curves of commonly used combination models: (**a**) Maxwell; (**b**) Kelvin; (**c**) Modified Kelvin; (**d**) Poying-Thomson; (**e**) Burgers and Nishihara; (**f**) Bingham.

3.2. Model Selection

In the numerical simulation, choosing the appropriate constitutive model is one of the most concerning issues for researchers [39]. At present, the numerical calculation of tunnel creeps usually adopts the component combination model. Under different geological conditions, the selection methods of the creep model are also different [40]. The creep characteristics of each creep model in Section 3.2 needed to be analyzed, summarized, and compared with test or monitoring results to select a suitable creep model. In practical applications, direct screening and posterior exclusion methods are usually used to reflect the main deformation characteristics of rocks [41]. The posterior exclusion method requires field tests, while the direct screening method can obtain the deformation curve of the rock under the action of time through field monitoring data, so the direct screening method is adopted.

Optical fiber multipoint displacement meters are used to measure surrounding rock deformation. According to the field deformation monitoring results of the typical section, the displacement-time curve of the surrounding rock is drawn and fitted, and the results are shown in Figure 3. Compared with the creep curves in Figure 2, Burgers and Nishihara can reflect the deformation characteristics of the surrounding rock. However, when the stress level is low, Nishihara will show Kelvin creep characteristics, and it is more challenging to identify the parameters of Nishihara mentioned in Section 3.1. Therefore, Burgers is selected as the constitutive creep model of the tunnel surrounding rock.

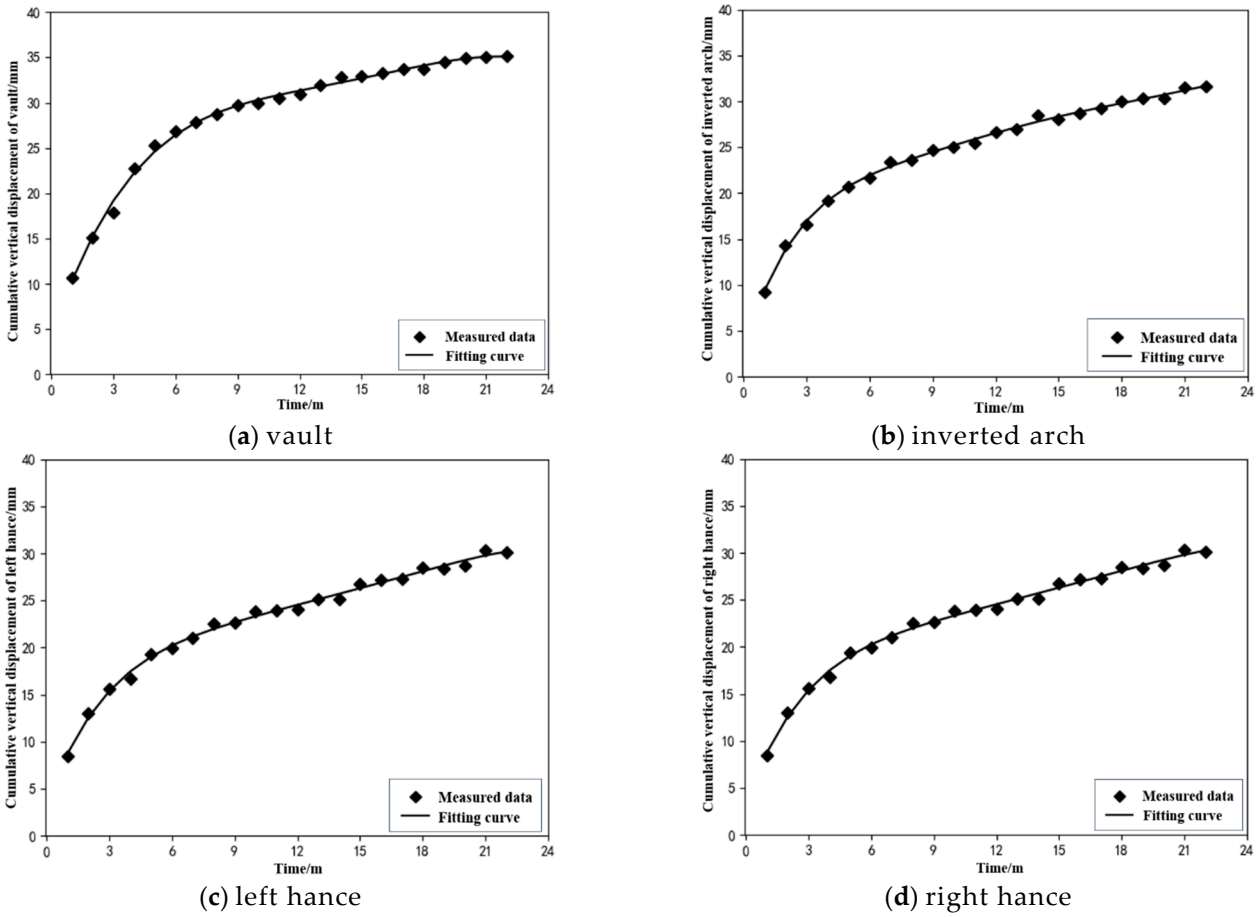

Figure 3. Displacement-time curve of surrounding rock.

3.3. Burgers Creep Model

Burgers is a four-parameter viscoelastic creep model formed by Kelvin and Maxwell in series [42], and its structure is shown in Figure 4.

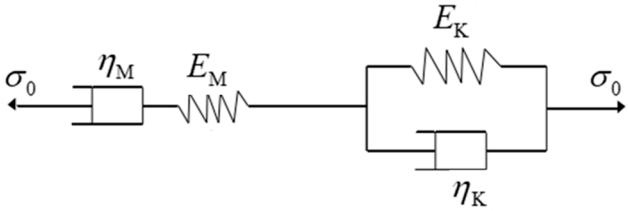

Figure 4. Structure of Burgers.

The constitutive equation of Maxwell is:

$$\varepsilon_M = \frac{\sigma_0}{E_M} + \frac{\sigma_0}{\eta_M} t \tag{1}$$

where σ_0 is the stress applied to the model; ε_M, E_M, and η_M represent the strain, elastic modulus, and viscosity coefficient of Maxwell, respectively.

The constitutive equation of Kelvin is:

$$\varepsilon_K = \frac{\sigma_0}{E_K}\left(1 - e^{-\frac{E_K}{\eta_K} t}\right)\eta_K \tag{2}$$

where σ_0 is the stress applied to the model; ε_K, E_K and η_K represent the strain, elastic modulus, and viscosity coefficient of Kelvin, respectively.

The total strain law should conform to the formula:

$$\varepsilon_B = \varepsilon_M + \varepsilon_K \tag{3}$$

where ε_B is the total strain of the component combination model.

According to the rules of the series, the stress σ_0 of Maxwell and Kelvin is the same. Combining Equations (2)–(4) to obtain the Burgers creep constitutive equation:

$$\varepsilon_B = \frac{\sigma_0}{E_M} + \frac{\sigma_0}{\eta_M} t + \frac{\sigma_0}{E_K}\left(1 - e^{-\frac{E_K}{\eta_K} t}\right) \tag{4}$$

4. Engineering Example

4.1. Project Overview

4.1.1. Geological Conditions

DT-HS project is a large-scale inter-basin water diversion project to solve the resource and engineering water shortage problems of the HuangShui River basin in Qinghai Province, as shown in see Figure 5. The diversion tunnel is the key control project and belongs to the deep-buried extra-long tunnel. The complexity of geological conditions is extremely rare in the Tunnel Boring Machine (TBM) hydraulic tunnel projects that have been completed and are under construction worldwide. The tunnel passes through more than 30 large and small faults, among which the largest faults, F5 and F4 (K17 + 192 − K16 + 088), are 1104 m wide, as shown in Figure 6.

Figure 5. DT-HS project.

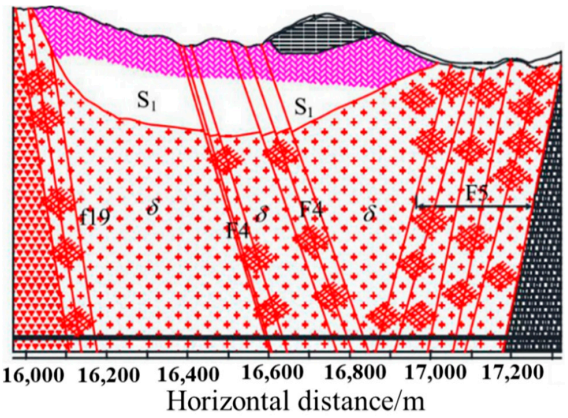

Figure 6. Engineering geologic profile.

According to the engineering geological report of the DT-HS project, the maximum horizontal principal stress is 21.1~22.1 MPa, the minimum horizontal principal stress is

12~14.2 MPa, and the vertical stress is 18.2 MPa~21.9 MPa. The maximum horizontal principal stress orientation is 307~317°, close to the NW direction and similar to the tunnel axis. Thus, σ_{xy}, σ_{yz}, and σ_{zx} can be set to 0. Papers related to the citation of the DT-HD project also confirm the feasibility of this method of taking values [43]. Hence, when calculating the initial stress field, σ_{xx} = 18.8 MPa, σ_{yy} = 25.8 MPa, σ_{zz} = 21.9 MPa, where y and z are parallel and perpendicular to the tunnel axis, respectively, as shown in Table 2.

Table 2. Ground stress field.

σ_{xx}/MPa	σ_{yy}/MPa	σ_{zz}/MPa	σ_{xy}/MPa	σ_{yz}/MPa	σ_{zx}/MPa
18.8	25.8	21.9	0.0	0.0	0.0

4.1.2. Excavation Methods and Blockage Accidents

The entrance floor elevation of the diversion tunnel is 2955.6 m, and the exit floor elevation is 2914.7 m. The tunnel is a pressureless diversion tunnel, with a length of 24.16 km, a maximum buried depth of 1100 m, and an average buried depth of 480 m. The export section is built by the TB593E/TS double shielded TBM from Germany. As shown in Figure 7, the length of the main engine was 12.5 m, and the diameter of the TBM excavation was 5930 mm. Precast quadrilateral reinforced concrete segments are used for lining.

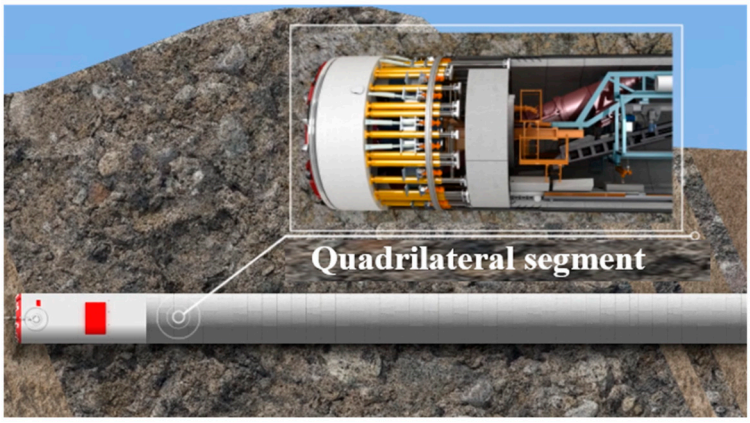

Figure 7. TB593E/TS TBM.

The surrounding rock is crushed, kaolinized, with low rock strength, and is seriously metamorphic of some rock. Blockage accidents have occurred more than ten times, as shown in Figure 8, and Table 3 summarizes the time, place, and reasons for the blockage accident.

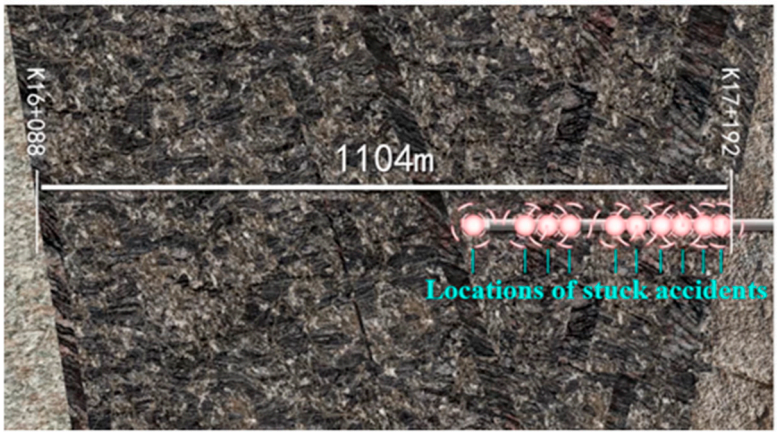

Figure 8. Locations of blockage accidents.

Table 3. Blockage accidents.

Order	Time	Location	Reasons
1	3 April 2008	K17 + 140	Convergence
2	30 April 2008	K17 + 135	Collapse and convergence
3	29 June 2008	K17 + 133	Collapse
4	3 September 2008	K17 + 117	Convergence
5	3 November 2008	K17 + 102	Collapse and convergence
6	24 December 2008	K17 + 086	Collapse and convergence
7	18 September 2009	K16 + 905	Collapse
8	18 October 2009	K16 + 881	Collapse and convergence
9	25 December 2009	K16 + 876	Collapse and convergence
10	23 July 2010	K16 + 775	Convergence

4.2. Numerical Model of Fault

The traditional methods for meshing cross-fault 3D numerical models are mainly divided into two types in Figure 9. The first one does not need much consideration about mesh shape and is automatically divided by mesh division software. The second is to consider the grid's shape and the fault's approximation boundary conditions and divide the regular grid according to the approximation boundary of the fault. On the other hand, the grid division method suggested in this work divides the rock body into regular grids first. This grid is then demarcated as a fault when more than half of it is within a fault, and else it is another rock body. The computation accuracy will be higher since the grid is more regular and situated closer to the real fault border. The specific discriminatory formula is as follows:

$$\frac{S_C}{S_F} \geq \frac{1}{2} \tag{5}$$

where S_C is the area of the grid that falls within the fault; S_F is the grid area.

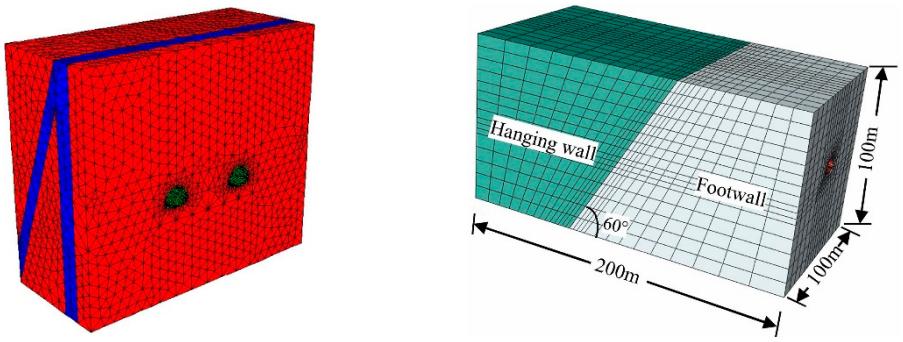

(**a**) (**b**)

Figure 9. The meshing methods for cross-fault 3D numerical model. (**a**) The first method [6]. (**b**) The second method [17].

In general, the boundary of the model can be divided into two categories: natural boundary and artificial boundary. The natural boundary refers to the boundary that should exist in the model itself in the actual engineering state, and this kind of boundary usually needs to be set when the engineering model is established. In contrast, the artificial boundary refers to the critical surface that exists around the engineering model after a certain engineering range is separated from the infinite geotechnical body. The model boundary in this paper is an artificial boundary. In order to make the geotechnical characteristics in the model consistent with actual engineering, certain constraints, such as displacements and stresses, are imposed on these boundaries before calculation. The advantage of this approach is that it does not need to build a complete underlying model, reducing the number of meshes while improving computational efficiency.

Choosing a reasonable model size also plays a vital role in ensuring the efficiency and accuracy of the calculation. Experimentally, the boundary of a deep underground tunnel model is generally 3~5 times the diameter of the tunnel [44]. Therefore, the calculation range of the model is 36 m × 36 m × 50 m, with horizontal coordinates (*x*-direction), vertical coordinates (*z*-direction), and extending tunnel axial direction (*y*-direction) of −18~18 m, −18~18 m, and 0~50 m, respectively. Meanwhile, the center point of the tunnel in section y = 0 m is the origin, the length of the fault is 10 m along the extension direction, and the included angle between the fault and the tunnel is 60. It is noteworthy that the model is modeled and gridded by HYPERMESH and converted to FLAC3D format by the HYPERMESH-FLAC3D program. The calculation model is divided by hexahedron grids, including 614400 elements and 637721 nodes. In order to ensure calculation accuracy, the grid size on and around the fault is refined, as shown in Figure 10.

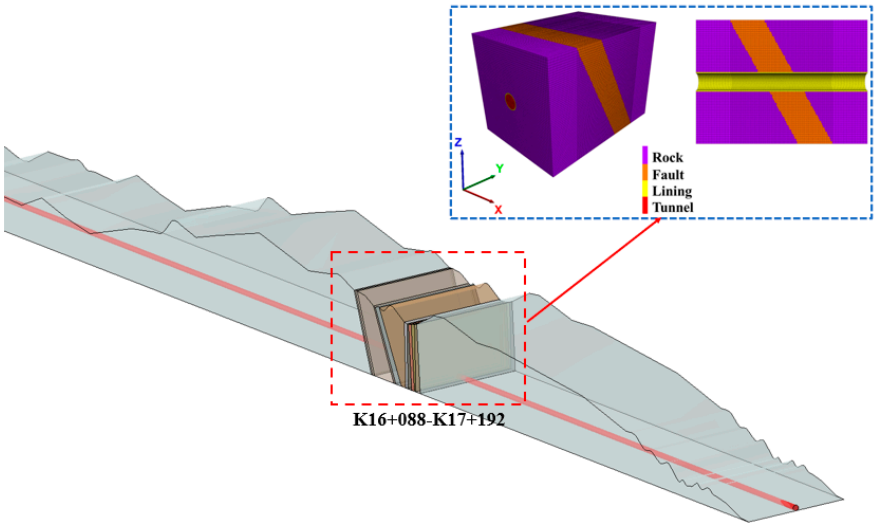

Figure 10. Fault-tunnel 3D Numerical Model.

The tunnel is circular with a diameter of 5 m, and segments with a width of 1.5 m and thickness of 0.35 m are used as linings. The segment concrete strength grade C40 and the impermeability grade WS are adopted. There are 6 pieces in each ring simulated by entity units. The specific physical and mechanical parameters are shown in Table 4.

Table 4. Physical and mechanical parameters of segment.

Elastic Modulus *E*/GPa	Poisson Ratio μ	Volumetric Weight γ/kN·m^{-3}	Outer Diameter *R*/m	Inner Diameter *r*/m	Thickness *t*/m	Longitudinal Length *L*/m
25	0.15	25	5.7	5	0.35	1.5

The boundary nodes are fixed in the direction parallel to the Y-Z plane (x = −18 m and x = 18 m) and the X-Z plane (y = 0 m and y = 50 m). The nodes at the bottom of the model (z = −18 m) are also fixed in the vertical direction (see Figure 11) [45–47].

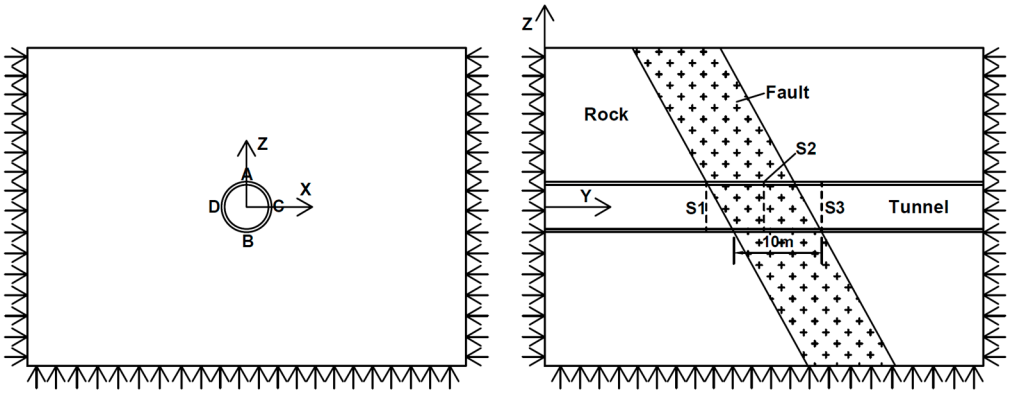

(a) Transverse boundary (**b**) Longitudinal boundary

Figure 11. Fixed boundary and monitoring locations.

In addition, Figure 10 presents the scheme of typical sections and monitoring points to study the influence of fault on the surrounding rock and segment lining. Three typical sections are set up in the tunnel model: (1) Section S1 (y = 18.5 m) placed at the entering zone of the fault, (2) Section S2 (y = 25 m) located in the middle of the fault, and Section S3 (y = 31.5 m) positioned completely separated from the fault. The measuring points A, B, C, and D are located along the tunnel and at the vault, inverted arch, right hance, and left hance of typical sections, respectively.

4.3. Simulation Parameters

The basic physical and mechanical parameters of the surrounding rock of F5 under the condition of measured ground stress are obtained using an intelligent inversion model and an integration analysis method combined with various machine learning algorithms [48]. Moreover, the other physical and mechanical parameters of creep analysis can be found in Table 5 [49,50].

Table 5. Physical and mechanical parameters of surrounding rock.

Type	Basic Physical and Mechanical Parameters					Creep Parameter			
						Maxwell		Kelvin	
	Volumetric Weight kN/m^3	Elastic Modulus E/GPa	Poisson Ratio μ	Internal Friction Angle Φ/(°)	Cohesion c/MPa	Elastic Modulus E_M/GPa	Viscosity Coefficient η_M/GPa·h	Elastic Modulus E_K/GPa	Viscosity Coefficient η_K/GPa·h
Rock	27.0	14.2	0.30	32.5	1	4	75	6	80
Fault	21.7	3.8	0.35	17.0	20	2	48	3	55

5. Results and Discussion

5.1. Creep Analysis during Construction

During excavation, the surrounding rock will produce instantaneous strain and creep deformation under the time effect. Therefore, after the initial stress calculation is completed, the Burgers creep constitutive model is adopted for calculation, and the creep deformation of the surrounding rock is fully considered.

By sorting out the calculation results, the longitudinal deformation profile (LDP) of the surrounding rock at monitoring points during construction is drawn, as shown in Figure 12. The LDP at the vault, inverted arch, and hance have similar overall changes. This shows that the displacement value increases at first and then decreases along the excavation direction. The maximum displacement segments of all monitoring points of the surrounding rock are also found to be located at fault. Moreover, the maximum displacement section does not appear in the middle of the fault, but it is on the vault, hance, and inverted arch in turn due to a certain included angle between the fault and the tunnel. The maximum vertical

displacements of the vault and the inverted arch are 8.74 cm at y = 22.75 m and 9.41 cm at y = 28.75 m, respectively. On the other hand, the maximum horizontal displacement of hance is 8.14 cm at y = 25.75 m.

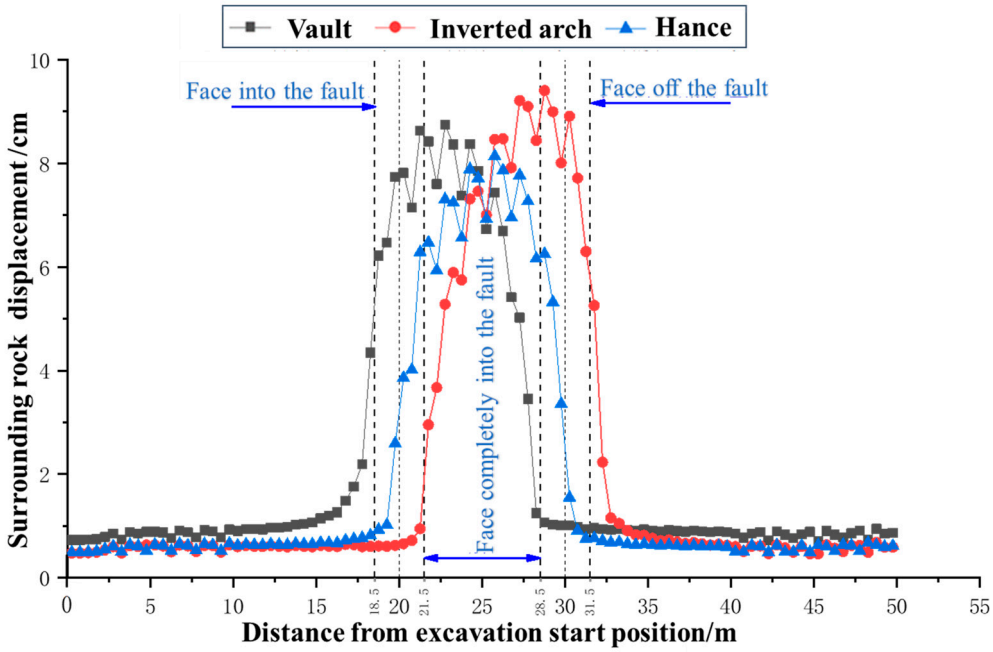

Figure 12. LDP of surrounding rock at monitoring points during construction.

According to the distance between the tunnel face and the fault from far to near, the deformation of the surrounding rock can be divided into small deformation, gradually increasing, and rapidly increasing, respectively. This phenomenon indicates that excavation near the fault is affected by the fault. The deformation of the surrounding rock suddenly increased near the fault, and hence, the tunnel structure is prone to collapse. However, it is impossible to judge whether there is a fault in front by monitoring the deformation of the surrounding rock in real tunnel construction. Subsequently, geological forecasting and reinforcing the surrounding rock in advance is necessary. Otherwise, the influence scope is about one time the tunnel diameter away from the fault, and the closer to the fault, the greater the influence. Since the vault enters the fault first, the displacement of the vault is affected by the fault first, followed by the hance, and finally, the inverted arch. Therefore, the tunnel face should be pre-reinforced at least one time the tunnel diameter from the fault.

Figure 13 shows the deformation gradient profile (DGP) of the surrounding rock. The deformation of the surrounding rock has a sudden change in the position of into and off the fault. Moreover, the deformation gradient of the surrounding rock in the fault is relatively large. At the fault's entry, the vault's maximum deformation gradient is 3.34 cm. Opposite, it is 4.21 and 3.01 cm of the inverted arch and hance, respectively, at the exit of the fault. This change increases the risk of uncoordinated deformation between the surrounding rock and the tunnel structure, and it is easy to cause damage to the tunnel structure.

According to the allowable longitudinal deflection or angular deformation of tunnel structure, the design idea of the segmented tunnel lining with flexible joints crossing the fault area can be adopted. That is to say, tunnel lining is divided into several segmented tunnel linings along the longitudinal direction, and the flexible joints are installed between the segmented tunnel linings and connected like a chain hinge. Therefore, the flexible joints hinder the axial transmission of segment lining deformation and reduce damage to the lining structure. In addition, the segment linings with flexible joints could make the structure localize damage to improve the dislocated performance of the whole tunnel through fault.

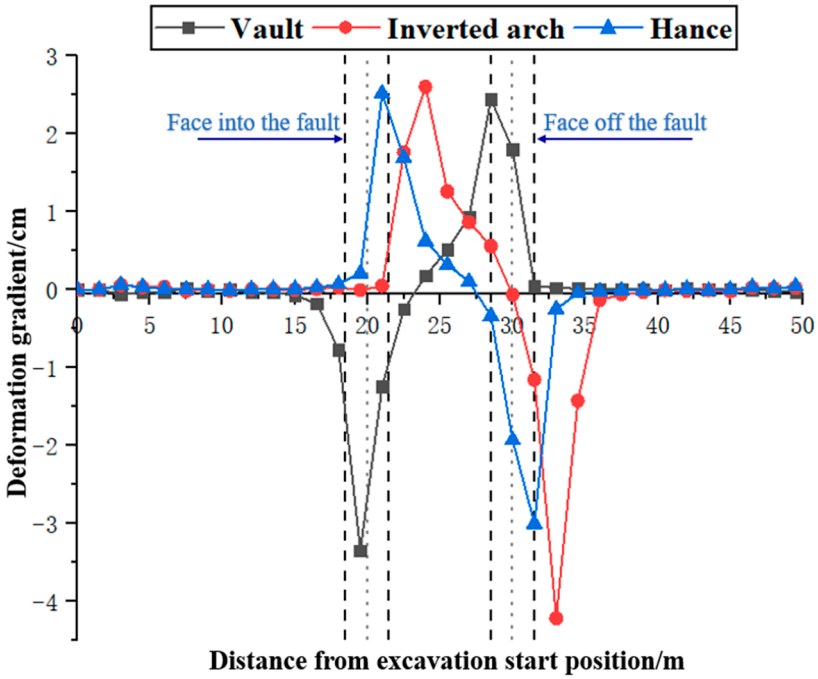

Figure 13. DGP of surrounding rock during construction.

5.2. Creep Analysis during Operation

5.2.1. Cumulative Displacement Curves of Surrounding Rock

Figure 14 shows the cumulative displacement profile (CDP) of the surrounding rock at monitored sites after creep calculation for 100 years. The maximum cumulative vertical displacement of the vault and inverted arch and the maximum cumulative horizontal displacement of hance are all within the fault. The greater the accumulated displacement and the faster the change means that the weak surrounding rock in the fault has stronger creep characteristics. This phenomenon will have an impact on the surrounding rock within one time of the tunnel diameter outside the fault. Consequently, during the operation, it is necessary to focus on monitoring the surrounding rock within the fault and strengthen the monitoring of the rock mass within one time of the tunnel diameter outside the fault.

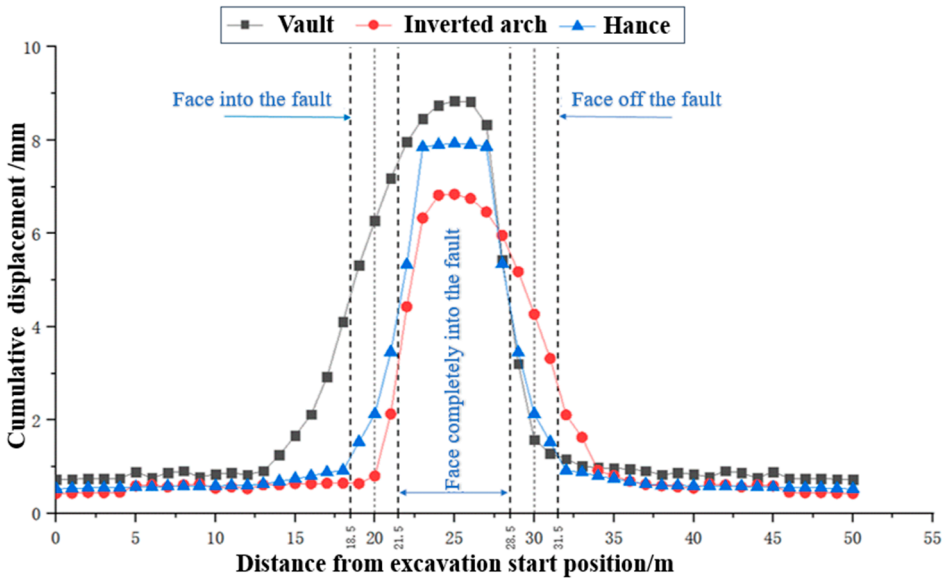

Figure 14. CDP of surrounding rock at monitoring sites during operation.

In addition, the inlet and outlet of fault at the vault and inverted arch are not symmetrical with respect to Section S2 and their cumulative vertical displacement curves are also asymmetrical. This trend occurred because of a significant included angle between the fault and the tunnel (i.d. 60). The cumulative displacement curve of the tunnel face near the entrance of the fault also changes more slowly than that of the tunnel face near the exit of the fault since the vault first contacts the fault. The inlet and outlet of fault at the hance take Section S2 as the symmetry plane so that the accumulated horizontal displacement curves are symmetrical.

5.2.2. Displacement Analysis of Segment Linings

The vertical displacement contour of Section S1 and Section S3 segment linings are presented in Figure 15. In Section S1, the vertical deformation of the segment lining at the vault is mainly settlement increasing continuously from 0.98 mm in the first year to 6.12 mm in the 100th year, with a total increase of 5.14 mm. The growth rate is relatively fast from the first year to the tenth year, and then it remains stable over time. The vertical deformation of segment lining at the inverted arch is also mainly uplift decreasing continuously (the settlement value increases) from 16.30 mm in the first year to 12.96 mm in the 100th year, with a total decreasing range of 3.34 mm. The rate of decline is rapid from the first year to the tenth year, and then it remains stable with time. More specifically, the changing trend of vertical displacement at the vault and inverted arch are basically the same under creep conditions, and the segment linings have a settlement trend as a whole. The horizontal displacement changes of the left and right hance segment lining are basically consistent. The maximum horizontal displacement occurs in the left and right hance and is symmetrically distributed on both sides. The displacement direction is developing towards the inside of the tunnel. Moreover, the horizontal displacement of left and right hance decreased from 11.28 to 10.34 mm from the first year to the 100th year with a total decrease rate of 8.33%. It declined rapidly in the previous decade and then stabilized.

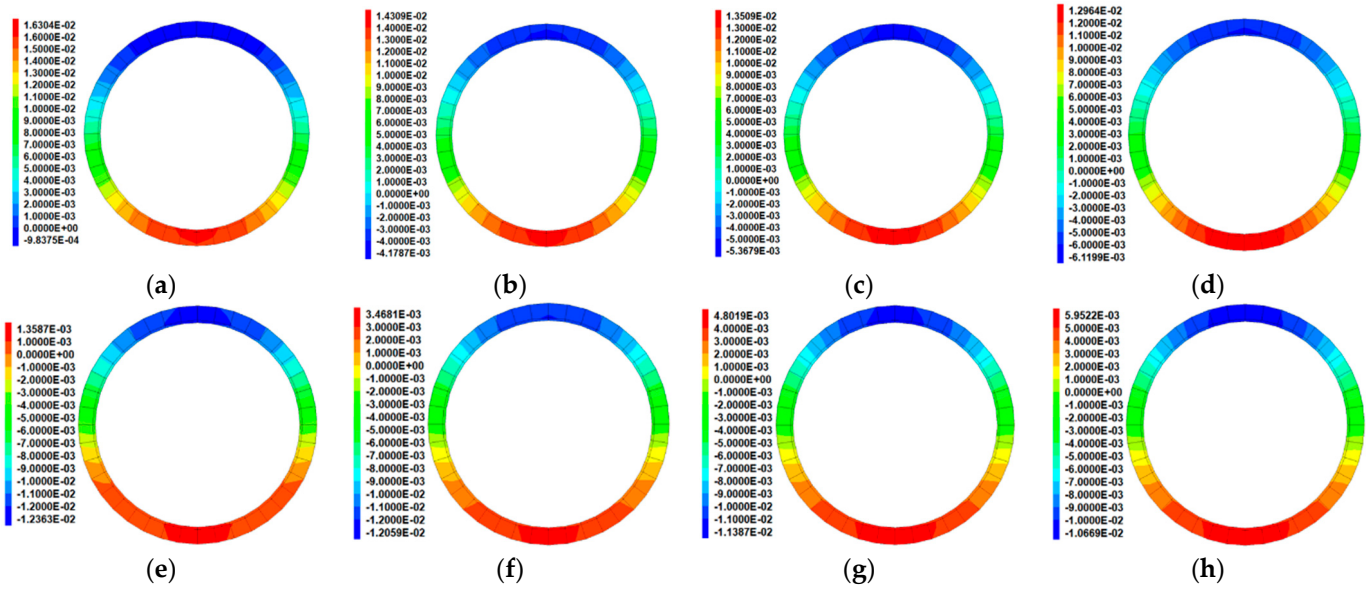

Figure 15. Vertical displacement of segment linings in Section S1 in: (**a**) 1st year; (**b**) 10th year; (**c**) 50th year; (**d**) 100th year; and Section S3 in: (**e**) 1st year; (**f**) 10th year; (**g**) 50th year; (**h**) 100th year.

In Section S3, the vertical deformation of segment lining at the vault is mainly settlement decreasing continuously (the uplift value increases) from 12.36 mm in the first year to 10.67 mm in the 100th year, with a total decreasing range of 1.69 mm. The decrease rate is relatively fast from the first year to the tenth year, and then it remains stable over time. Furthermore, the vertical deformation of segment lining at the inverted arch is mainly uplifted, increasing continuously from 1.36 mm in the first year to 5.59 mm in the 100th

year, with a total increase of 4.59 mm. The growth rate is relatively fast from the first year to the tenth year, and then it remains stable with time. Obviously, under creep conditions, the changing trend of vertical displacement at the vault and inverted arch are basically the same, and the segment linings have a rising trend as a whole. The horizontal displacement changes of the left and right hance segment lining are basically consistent. The maximum horizontal displacement occurs in the left and right hance and is symmetrically distributed on both sides. The displacement direction is developing towards the inside of the tunnel. The horizontal displacement of left and right hance decreased from 11.79 mm to 10.40 mm from the first year to the 100th year, with a total decrease rate of 11.79%. Moreover, the decrease in the horizontal displacement in Section S3 is greater than that in Section S1. It declined rapidly in the previous decade and then stabilized.

5.3. Comparative Analysis

5.3.1. Displacement Comparison of Segment Linings at Typical Sections

The overall variation of segment lining displacement in Section S1 and Section S3 is basically the same. Both change rapidly in the first ten years and then rapidly decrease. Be worth noting that the fault affects the vertical displacement of segment linings. Section S1 shows the vertical displacement of the vault and inverted arch developing downward because the fault is located above the tunnel. However, the vertical displacement of the vault is relatively large. In contrast, the vertical displacement of the inverted arch changes significantly, while the vertical displacement of the vault and inverted arch develops upward in Section S3, where the fault is located below the tunnel. The horizontal displacement of left and right hance segment linings decreases slightly, with the same decrescent magnitude in two sections. The development direction of lining horizontal displacement is inward, indicating that the fault has little influence on the horizontal displacement of segment linings.

Table 6 summarizes the displacement of different monitoring points at different times in Sections S1 and S3. The change rate of the surrounding rock is significant in the first 10 years, then decreases and remains stable. The vertical displacement is obviously higher than the horizontal displacement. Consequently, the influence of fault on the surrounding rock displacement is mainly vertical. In addition, the main direction of compression in gravity in situ stress field is vertical, and the creep of the surrounding rock also causes compression deformation of the strata. Thus, the overall deformation of the segment lining is compressed into the tunnel. However, the vertical displacement of the segment linings at the inverted arch of Section S1 and the vault of Section S3 develop towards the outside of the tunnel. This indicates that the creep of the surrounding rock in the fault also causes the compression deformation of the stratum, with a direction towards the outside of the fault.

Table 6. Displacement of different monitoring points at different times.

Position		Displacement/mm					Average Speed	
		1st Year	10st Year	100th Year	Previous 10 Years	Posterior 90 Years	Previous 10 Years	Posterior 90 Years
S1	Vault	0.98	4.18	6.12	3.20	1.32	0.356	0.015
	Inverted arch	16.30	14.3	12.96	2.00	1.34	0.222	0.015
	Hance	11.28	11.00	10.34	0.28	0.66	0.031	0.007
S3	Vault	12.36	12.08	10.67	0.28	1.41	0.031	0.016
	Inverted arch	1.36	3.47	5.95	2.11	2.48	0.234	0.028
	Hance	11.79	11.45	10.40	0.34	1.05	0.038	0.012

In general, the vertical displacement of the vault segment lining of Section S1 is the most obvious under creep effect. Figure 16 shows the research object and drawing of the displacement-time curve. The figure indicates that the creep deformation rate of segment lining is very large in the first 10 years, then drops suddenly. The deformation of segment

linings in the first 50 years accords with the deformation of the decay creep stage, while the deformation of segment lining in the last 50 years is in the steady creep stage.

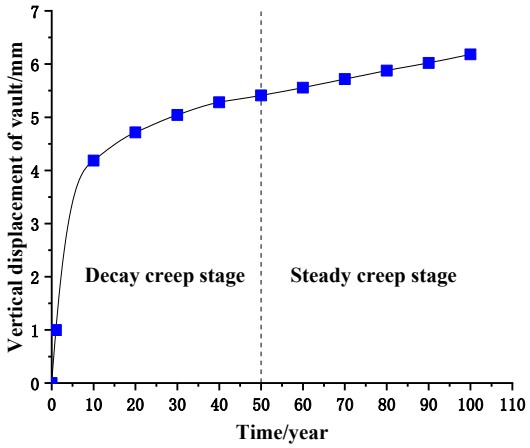

Figure 16. Vertical displacement of the vault segment lining.

5.3.2. Stress Comparison of Segment Linings at Typical Sections

Creep is the process in which the internal stress of the surrounding rock is constantly adjusted. In this section, the maximum principal stress contour of Section S1 and Section S3 segment linings are presented in Figure 17 to compare the stress of segment linings in typical sections. The maximum principal stress and minimum principal stress on the segment lining of Section S1 and Section S3 are basically the same. Both stresses are constantly changing and tend to increase over time. At the initial stage after the tunnel's completion, the stress growth rate of segment linings is relatively high. After a period of time, the stress growth rate gradually decreases, confirming the existence of the creep characteristics of the surrounding rock. Therefore, it shows that the creep of the surrounding rock has changed the stress of segment linings.

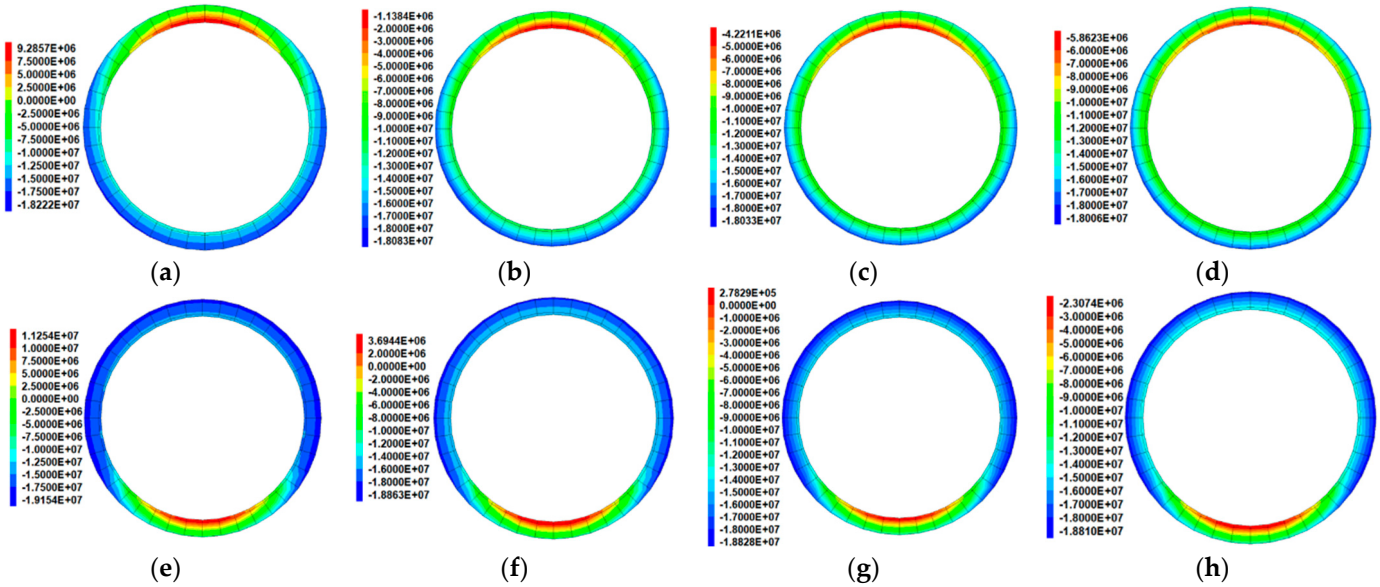

Figure 17. Maximum principal stress of segment lining at Section S1 in: (**a**) 1st year; (**b**) 10th year; (**c**) 50th year; (**d**) 100th year; and Section S3 in: (**e**) 1st year; (**f**) 10th year; (**g**) 50th year; (**h**) 100th year.

Considering the interaction between the surrounding rock and segment linings, the creep of the surrounding rock greatly impacts the stress of segment linings in the first 10 years after the completion of tunnel construction. Subsequently, a period of 10 to 50 years

is a process of adjustment. Thereafter, the lining stress gradually stabilizes. Moreover, the maximum principal stress of vault segment lining slowly changes from a tensile state to a pressure state, specifically where the location of the fault is above the tunnel (i.e., Section S1). In contrast, the maximum principal stress of tunnel segment lining gradually changes from tensile stress to compressive stress where the location of the fault is under the tunnel (i.e., Section S3). The results show that the fault has an influence on the stress state of segment linings, which is the same as the changing trend of displacement of segment linings.

6. Conclusions

A three-dimensional cross-fault numerical model of the DT-HS project is established to study the influence of fault on surrounding rocks and segment linings during tunnel construction and operation under the creep effect. The conclusions are as follows:

(1) Certain differences in the stress distribution of surrounding rocks are found in the first 10 years after the completion of tunnel construction. More specifically, the creep of the surrounding rock greatly influences the stress of segment linings within this period. In the following 10~50 years, the creep of surrounding rocks continuously adjusts and affects the stress of segment linings. Since then, the stress on the lining is gradually stabilized.

(2) The vertical displacement is obviously higher than the horizontal displacement. Consequently, the influence of fault on the displacement of the surrounding rock is mainly vertical. Meanwhile, the creep of the surrounding rock in the fault causes the compression deformation of the stratum, with a direction towards the outside of the fault. Consequently, attention should be paid to monitoring the deformation of the segment linings at the vault and the inverted arch. In addition, the design idea of the segmented tunnel lining with flexible joints crossing the fault area can also be adopted.

(3) The fault affects the stress state of segment linings. Moreover, the maximum principal stress of vault segment linings slowly changes from a tensile state to a pressure state when the fault is above the tunnel at Section S1. However, the maximum principal stress of tunnel segment lining gradually changes from tensile stress to compressive stress when the fault is under the tunnel at Section S3.

(4) The fault directly affects the rock mass characteristics near the fault with a radius of influence of about one time the tunnel diameter from the fault. Generally, the closer to the fault, the greater the influence. The inlet and outlet of fault at the vault and inverted arch are not symmetrical with respect to the S2 section resulting in their asymmetrical cumulative vertical displacement curves. Nevertheless, the inlet and outlet of fault at the hance take the S2 section as the symmetry plane so that the accumulated horizontal displacement curves are symmetrical. In this case, geological forecasting is necessary, and the surrounding rock should be pre-reinforced one time the tunnel diameter from the fault. After the completion of the tunnel construction, we should focus on monitoring the structure, which is one time the tunnel diameter from the fault or in the fault in the first 50 years, and adopt a higher monitoring frequency in the first 10 years to ensure that the deformation of the surrounding rock is within the controllable range.

Author Contributions: Conceptualization, Y.H.; methodology, Y.H.; software, Y.H.; formal analysis, Y.H.; resources, X.S.; writing—review and editing, M.Z. and X.S.; funding acquisition, X.S.; formal analysis, X.S.; validation, X.S. All authors have read and agreed to the published version of the manuscript.

Funding: This research was funded by the National Natural Science Foundation of China (51879185), and the Natural Science Foundation of Qinghai Province in China (2020-SF-138).

Institutional Review Board Statement: Not applicable.

Informed Consent Statement: Not applicable.

Data Availability Statement: Not applicable.

Acknowledgments: The authors gratefully acknowledge the financial support from the National Natural Science Foundation of China (51879185) and the Natural Science Foundation of Qinghai Province in China (2020-SF-138). The authors also wish to thank the editors of Buildings for the work.

Conflicts of Interest: The authors declare no conflict of interest.

References

1. Yan, G.; Gao, B.; Shen, Y.; Zheng, Q.; Fan, K.; Huang, H. Shaking table test on seismic performances of new designed joints for mountain tunnels crossing faults. *Adv. Struct. Eng.* **2020**, *23*, 248–262. [CrossRef]
2. Yan, G.; Shen, Y.; Gao, B.; Zheng, Q.; Fan, K.; Huang, H. Damage evolution of tunnel lining with steel reinforced rubber joints under normal faulting: An experimental and numerical investigation. *Tunn. Undergr. Space Technol.* **2020**, *97*, 103223. [CrossRef]
3. Wu, D.; Zhang, Y.; Zhao, R.; Deng, T.; Zheng, Z. A coupled thermal-hydraulic-mechanical application for subway tunnel. *Comput. Geotech.* **2021**, *140*, 104467. [CrossRef]
4. Yu, H.T.; Chen, J.T.; Bobet, A.; Yuan, Y. Damage observation and assessment of the Longxi tunnel during the Wenchuan earthquake. *Tunn. Undergr. Space Technol.* **2016**, *54*, 102–116. [CrossRef]
5. Huang, J.Q.; Zhao, M.; Du, X.L. Non-linear seismic responses of tunnels within normal fault ground under obliquely incident P waves. *Tunn. Undergr. Space Technol.* **2017**, *61*, 26–39. [CrossRef]
6. Gao, C.L.; Zhou, Z.Q.; Yang, W.M.; Lin, C.J.; Li, L.P.; Wang, J. Model test and numerical simulation research of water leakage in operating tunnels passing through intersecting faults. *Tunn. Undergr. Space Technol.* **2019**, *94*, 103134. [CrossRef]
7. Anastasopoulos, I.; Gerolymos, N.; Drosos, V.; Georgarakos, T.; Kourkoulis, R.; Gazetas, G. Behaviour of deep immersed tunnel under combined normal fault rupture deformation and subsequent seismic shaking. *Bull. Earth. Eng.* **2008**, *6*, 213–239. [CrossRef]
8. Wang, Z.Z.; Zhang, Z. Seismic damage classification and risk assessment of mountain tunnels with a validation for the 2008 Wenchuan earthquake. *Soil Dyn. Earthq. Eng.* **2013**, *45*, 45–55. [CrossRef]
9. Zhang, H.J.; Wang, Z.Z.; Lu, F.; Xu, G.Y.; Qiu, W.G. Analysis of the displacement increment induced by removing temporary linings and corresponding countermeasures. *Tunn. Undergr. Space Technol.* **2018**, *73*, 236–243. [CrossRef]
10. Su, L.J.; Liu, H.Q.; Yao, G.C.; Zhang, J.L. Experimental study on the closed-cell aluminum foam shock absorption layer of a high-speed railway tunnel. *Soil Dyn. Earthq. Eng.* **2019**, *119*, 331–345. [CrossRef]
11. Wang, Z.Z.; Jiang, Y.J.; Zhu, C.A. Seismic energy response and damage evolution of tunnel lining structures. *Eur. J. Environ. Civ. Eng.* **2019**, *23*, 758–770. [CrossRef]
12. Wang, Z.Z.; Jiang, L.; Gao, Y. Shaking table test of seismic response of immersed tunnels under effect of water. *Soil Dyn. Earthq. Eng.* **2019**, *116*, 436–445. [CrossRef]
13. Sabagh, M.; Ghalandarzadeh, H. Centrifugal modeling of continuous shallow tunnels at active normal faults intersection. *Transp. Geotech.* **2020**, *22*, 100325. [CrossRef]
14. Yang, Z.; Lan, H.; Zhang, Y.; Gao, X.; Li, L. Nonlinear dynamic failure process of tunnel-fault system in response to strong seismic event. *J. Asian Earth Sci.* **2013**, *64*, 125–135. [CrossRef]
15. Cai, Q.P.; Peng, J.M.; Ng, C.W.W. Centrifuge and numerical modelling of tunnel intersected by normal fault rupture in sand. *Comput. Geotech.* **2019**, *111*, 137–146. [CrossRef]
16. Shen, Y.S.; Wang, Z.Z.; Yu, J.; Zhang, X.; Gao, B. Shaking table test on flexible joints of mountain tunnels passing through normal fault. *Tunn. Undergr. Space Technol.* **2020**, *98*, 103299. [CrossRef]
17. Zeng, G.; Geng, P.; Guo, X.; Li, P.; Wang, Q.; Ding, T. An anti-fault study of basalt fiber reinforced concrete in tunnels crossing a stick-slip fault. *Soil Dyn. Earthq. Eng.* **2021**, *148*, 106687. [CrossRef]
18. Huang, F.; Zhu, H.; Xu, Q.; Cai, Y.; Zhuang, X. The effect of weak interlayer on the failure pattern of rock mass around tunnel—Scaled model tests and numerical analysis. *Tunn. Undergr. Space Technol.* **2013**, *35*, 207–218. [CrossRef]
19. Baziar, M.H.; Nabizadeh, A.; Lee, C.J.; Hung, W.Y. Centrifuge modeling of interaction between reverse faulting and tunnel. *Soil Dyn. Earthq. Eng.* **2014**, *65*, 151–164. [CrossRef]
20. Baziar, M.H.; Nabizadeh, A.; Mehrabi, R.; Lee, C.J.; Hung, W.Y. Evaluation of underground tunnel response to reverse fault rupture using numerical approach. *Soil Dyn. Earthq. Eng.* **2016**, *83*, 1–17. [CrossRef]
21. Zhang, Z.Q.; Chen, F.F.; Li, N. Influence of fault on the surrounding rock stability of a tunnel: Location and thickness. *Tunn. Undergr. Space Technol.* **2017**, *61*, 1–11. [CrossRef]
22. Sabagh, M.; Ghalandarzadeh, H. Numerical modelings of continuous shallow tunnels subject to reverse faulting and its verification through a centrifuge. *Comput. Geotech.* **2020**, *128*, 103813. [CrossRef]
23. Zaheri, M.; Ranjbarnia, M.; Dias, D.; Oreste, P. Performance of segmental and shotcrete linings in shallow tunnels crossing a transverse strike-slip faulting. *Transp. Geotech.* **2020**, *23*, 100333. [CrossRef]
24. Yao, C.; He, C.; Takemura, J.; Feng, K.; Guo, D.; Huang, X. Active length of a continuous pipe or tunnel subjected to reverse faulting. *Soil Dyn. Earthq. Eng.* **2021**, *148*, 106825. [CrossRef]
25. Xu, G.W.; He, C.; Yang, Q.H.; Wang, B. Progressive failure process of secondary lining of a tunnel under creep effect of surrounding rock. *Tunn. Undergr. Space Technol.* **2019**, *90*, 76–98. [CrossRef]
26. Liu, Y.; Hou, S.; Li, C.; Zhou, H.; Jin, F.; Qin, P.; Yang, Q. Study on support time in double-shield TBM tunnel based on self-compacting concrete backfilling material. *Tunn. Undergr. Space Technol.* **2020**, *96*, 103212. [CrossRef]

27. Liu, B.G.; Song, Y.; Chu, Z.F. Time-dependent safety of lining structures of circular tunnels in weak rock strata. *Int. J. Min. Sci. Technol.* **2021**, *32*, 323–334. [CrossRef]
28. Cui, L.; Zheng, J.J.; Sheng, Q.; Pan, Y. A simplified procedure for the interaction between fully-grouted bolts and rock mass for circular tunnels. *Comput. Geotech.* **2019**, *106*, 177–192. [CrossRef]
29. Zhang, W.; Han, L.; Gu, X.; Wang, L.; Chen, F.; Liu, H. Tunneling and deep excavations in spatially variable soil and rock masses: A short review. *Undergr. Space* **2020**, *7*, 380–407. [CrossRef]
30. Kabwe, E.; Karakus, M.; Chanda, E.K. Creep constitutive model considering the overstress theory with an associative viscoplastic flow rule. *Comput. Geotech.* **2020**, *124*, 103629. [CrossRef]
31. Taheri, S.R.; Pak, A.; Shad, S.; Mehrgini, B.; Razifar, M. Investigation of rock salt layer creep and its effects on casing collapse. *Int. J. Min. Sci. Technol.* **2020**, *30*, 357–365. [CrossRef]
32. Zhao, Y.; Wang, Y.; Wang, W.; Wan, W.; Tang, J. Modeling of non-linear rheological behavior of hard rock using triaxial rheological experiment. *Int. J. Rock Mech. Min. Sci.* **2017**, *93*, 66–75. [CrossRef]
33. Paraskevopoulou, C.; Diederichs, M. Analysis of time-dependent deformation in tunnels using the Convergence-Confinement Method. *Tunn. Undergr. Space Technol.* **2018**, *71*, 62–80. [CrossRef]
34. Fahimifar, A.; Tehrani, F.M.; Hedayat, A.; Vakilzadeh, A. Analytical solution for the excavation of circular tunnels in a visco-elastic Burger's material under hydrostatic stress field. *Tunn. Undergr. Space Technol.* **2010**, *25*, 297–304. [CrossRef]
35. Zhao, D.P.; Jia, L.L.; Wang, M.N.; Wang, F. Displacement prediction of tunnels based on a generalised Kelvin constitutive model and its application in a subsea tunnel. *Tunn. Undergr. Space Technol.* **2017**, *54*, 29–36. [CrossRef]
36. Lee, C.L.; Shou, K.J.; Chen, S.S.; Zhou, W.C. Numerical analysis of tunneling in slates with anisotropic time-dependent behavior. *Tunn. Undergr. Space Technol.* **2019**, *84*, 281–294. [CrossRef]
37. Chu, Z.F.; Wu, Z.J.; Liu, B.G.; Liu, Q.S. Coupled analytical solutions for deep-buried circular lined tunnels considering tunnel face advancement and soft rock rheology effects. *Tunn. Undergr. Space Technol.* **2019**, *94*, 103111. [CrossRef]
38. Zhang, Z.; Huang, M.; Zhang, C.; Jiang, K.; Lu, M. Time-domain analyses for pile deformation induced by adjacent excavation considering influences of viscoelastic mechanism. *Tunn. Undergr. Space Technol.* **2019**, *85*, 392–405. [CrossRef]
39. Gu, X.; Chen, F.; Zhang, W.; Wang, Q.; Liu, H. Numerical investigation of pile responses induced by adjacent tunnel excavation in spatially variable clays. *Undergr. Space* **2021**, *7*, 911–927. [CrossRef]
40. Xu, G.W.; Gutierrez, M. Study on the damage evolution in secondary tunnel lining under the combined actions of corrosion degradation of preliminary support and creep deformation of surrounding rock. *Transp. Geotech.* **2021**, *27*, 100501. [CrossRef]
41. Yang, F.; Zhang, C.; Zhou, H.; Liu, N.; Zhang, Y.; Azhar, M.U.; Dai, F. The long-term safety of a deeply buried soft rock tunnel lining under inside-to-outside seepage conditions. *Tunn. Undergr. Space Technol.* **2017**, *67*, 132–146. [CrossRef]
42. Zhang, J.Z.; Zhou, X.P. Time-dependent jamming mechanism for Single-Shield TBM tunneling in squeezing rock. *Tunn. Undergr. Space Technol.* **2017**, *69*, 209–222. [CrossRef]
43. Xing, H.; Quan-sheng, L.; Xing-xin, P.; Guang-feng, L.; Lai, W. Analysis and comprehensive prevention-control for TBM jamming induced by squeezing deformation of surrounding rock around water diversion tunnel from Datong River into Huangshui River. *Rock Soil Mech.* **2017**, *38*, 2962–2972. (In Chinese)
44. Su, K.; Zhang, Y.J.; Chang, Z.H.; Wu, H.G.; Wang, T.; Zhou, W. Transverse extent of numerical model for deep buried tunnel excavation. *Tunn. Undergr. Space Technol.* **2019**, *84*, 373–380. [CrossRef]
45. Zhang, L.; Zhao, X.; Yan, X.; Yang, X. A new finite element model of buried steel pipelines crossing strike-slip faults considering equivalent boundary springs. *Eng. Struct.* **2016**, *123*, 30–44. [CrossRef]
46. Zhang, L.; Zhao, X.; Yan, X.; Yang, X. Elastoplastic analysis of mechanical response of buried pipelines under strike-slip faults. *Int. J. Geomech.* **2016**, *17*, 04016109. [CrossRef]
47. Ziaei, A.; Ahangari, K. The effect of topography on stability of shallow tunnels case study: The diversion and conveyance tunnels of Safa Dam. *Transp. Geotech.* **2018**, *14*, 126–135. [CrossRef]
48. He, Y.; Sun, X.; Zhang, Y.; Guo, H.; Li, Q. Intelligent fusion model and analysis method for rock parameter inversion of water diversion tunnel. *J. Hydroelectr. Eng.* **2021**, *40*, 114–126. (In Chinese)
49. Fu, J.; Dong, H.Z.; Ding, X.L.; Zhang, C.J. Study of aging characteristics of soft surrounding rock in deep tunnel with high ground stress. *Rock Soil Mech.* **2011**, *32*, 444–448. (In Chinese)
50. Su, L.J.; Weng, J.L.; Lu, W.B. Stability analysis of 1000 m-deep-buried tunnel under high geostress entironment and its engineering application. *Rock Soil Mech.* **2008**, *29*, 221–226. (In Chinese)